energies

MDPI

Article

Numerical Modeling of Oxygen Carrier Performances ($NiO/NiAl_2O_4$) for Chemical-Looping Combustion

Lucia Blas [1], Patrick Dutournié [2], Mejdi Jeguirim [2,*], Ludovic Josien [2], David Chiche [3], Stephane Bertholin [3] and Arnold Lambert [3]

1 LGRE, Laboratoire Gestion des Risques, Environnement 3 bis, rue Alfred Werner, 68093 Mulhouse, France; Lucia.blas@uha.fr

2 IS2M, Institut de Sciences des Matériaux de Mulhouse, UMR 7361 CNRS, Université de Strasbourg, Université de Haute Alsace, 3 bis, rue Alfred Werner, 68098 Mulhouse CEDEX, France; Patrick.dutournie@uha.fr (P.D.); ludovic.josien@uha.fr (L.J.)

3 IFP Energies Nouvelles, Rond-Point de l'échangeur de Solaize, BP 3, 69360 Solaize, France; david.chiche@ifpen.fr (D.C.); stephane.bertholin@ifpen.fr (S.B.); arnold.lambert@ifpen.fr (A.L.)

* Correspondence: mejdi.jeguirim@uha.fr; Tel.: +33-3-89-60-86-61; Fax: +33-3-89-60-87-99

Academic Editor: Vasily Novozhilov

Received: 3 May 2017; Accepted: 20 June 2017; Published: 28 June 2017

Abstract: This work was devoted to study experimentally and numerically the oxygen carrier ($NiO/NiAl_2O_4$) performances for Chemical-Looping Combustion applications. Various kinetic models including Shrinking Core, Nucleation Growth and Modified Volumetric models were investigated in a one-dimensional approach to simulate the reactive mass transfer in a fixed bed reactor. The preliminary numerical results indicated that these models are unable to fit well the fuel breakthrough curves. Therefore, the oxygen carrier was characterized after several operations using Scanning Electronic Microscopy (SEM) coupled with equipped with an energy dispersive X-ray spectrometer (EDX). These analyses showed a layer rich in nickel on particle surface. Below this layer, to a depth of about 10 µm, the material was low in nickel, being the consequence of nickel migration. From these observations, two reactive sites were proposed relative to the layer rich in nickel (particle surface) and the bulk material, respectively. Then, a numerical model, taking into account of both reactive sites, was able to fit well fuel breakthrough curves for all the studied operating conditions. The extracted kinetic parameters showed that the fuel oxidation was fully controlled by the reaction and the effect of temperature was not significant in the tested operating conditions range.

Keywords: NiO reactivity; nickel migration; chemical looping combustion; fixed bed reactor; modelling

1. Introduction

In the current environmental context, greenhouse gas emissions should be limited to stabilize or to reduce global warming. Among the various causes, fossil fuel combustion contributes greatly to this phenomenon [1]. Hence, the limitation of greenhouse gas emissions through CO_2 separation, capture and sequestration becomes necessary. Several alternatives [2,3] have been studied, including geological storage, chemical storage, replanting programs and urban forests. The major drawback of these issues is the requirement of flue gas treatment to separate carbon dioxide. Indeed this step is energy intensive and jeopardizes the processes sustainability. To avoid this scenario, indirect combustion can be an alternative solution. In particular, Chemical-Looping Combustion (CLC) seems to be a promising option [4,5]. CLC consists in a combustion process that occurs in two steps with oxygen provided by an oxygen carrier (OC). During the first step, the fuel is oxidized by the oxygen carrier while in the second step, the oxygen carrier is re-oxidized by air [6]. The major advantage

of this technology is a flue gas composition out of the first step which consists entirely of water vapor and carbon dioxide. After water vapor condensation, the CO_2 can be used or sequestered. In addition, the second step of the process uses air to re-oxidize the oxygen carrier and emits only oxygen depleted air. From an environmental point of view, this technology is innovative and provides energy with greenhouse gas emission-free and even negative contribution for combustion of biomass and biogas [7,8]. The core technologies of CLC processes are fluidized or packed bed reactors. The first one consists of two interconnected fluidized beds [9], providing the reduction and the re-oxidation of the oxygen carrier, respectively. It operates continuously, but the circulation of the oxygen carrier leads to aggregation phenomena. The second technology is operating batch-wise, with the alternative injection of the different (oxidation/reduction) gases [10]. This technology requires an intermediate step (injection of non-reactive gas) to avoid the simultaneous presence of fuel and air in the reactor. The development of this technology (strategic focus for CLC efficiency) requires finding suitable oxygen carrier with good mechanical properties, reactivity and stability. The oxygen carrier generally consists in a metal oxide (based on Ni, Fe, Mn, Cu, ...) and a binder (generally porous alumina, silica, titania, zirconia, ...). The porous binder provides better mechanical, thermal and chemical properties, limiting agglomeration and attrition. Among these oxygen carriers and binders, the academic community deemed $NiO/NiAl_2O_4$ to be efficient and a reference material. This OC is highly thermally and mechanically stable and is very reactive. For these different reasons, this OC was widely used in laboratory studies. However, previous studies showed that the binder can react with fuel and lose partly its properties [11–13].

As previously observed [14], the binder can, in some cases, increase the global reactivity of the oxygen carrier. Indeed, the amount of metal oxide (NiO in this study) increases as operation proceeds (separation of the $NiAl_2O_4$ phase to NiO and Al_2O_3). In other cases, a migration of Ni metal is observed, leading to the formation of a Ni-rich layer coating the particle surface. This layer enables aggregation and sintering phenomena and decreases the global performance.

In addition to numerous experimental studies, few investigations were devoted to reaction kinetics of both reduction and re-oxidation. Two major model families were used namely unreacted shrinking core and nucleation-growth models [15]. These kinetic models are implemented in heat and mass transfer modelling to develop numerical tools able to simulate the whole process. Furthermore, numerical investigations may both study the OC behaviour and the phenomena occurring at the particle scale. In particular, several studies are devoted to the study of quasi industrial pilot plant. For example, Ohlemüller et al. [16] have numerically investigated coal CLC and validated with experimental 100 kW_{th} tests. Wang et al. [17] have simulated coal CLC in a circulating fluidized bed reactor via a 3D approach. Alobaid et al. [18] have used a 3D approach to simulate a 1 MW CLC pilot plant. For this, they have used Fluent software to model 3D momentum, mass and heat balances in a fluidized reactor. Studies relative to the numerical study of packed bed reactors [10] are fewer because the technology and the operation are more complicated than the fluidized bed reactor from an industrial point of view (operation in batch process). But from an academic point of view, this technology is very interesting owing to the simplification of the mathematical modelling [19,20], especially the fluid and OC dynamics.

In this work, different kinetic models are used to simulate experimental results of chemical-looping combustion of carbon monoxide in a fixed-bed reactor. Carbon monoxide is used as fuel because the combustion can be summarised in a global equation and avoid presence of water, deposited carbon, Hydrogen... that can significantly modify OC performances and act on catalytic properties, particle agglomeration, sintering... [21]. The kinetic models are input into a 1D-unsteady model to describe experimental breakthrough curves. Experimental and numerical results are compared and discussed with regards to characterization results.

2. Experimental Part

2.1. Material

The metal oxide used in this study is nickel oxide. In order to obtain good mechanical properties, the metal oxide is mixed with a binder (nickel aluminate 40 wt %). The particles were supplied by IFP Energies Nouvelles (Solaize, France) and obtained by granulation (with a Guedu granulator). The oxygen carrier was calcined at 1200 °C during 2 h, under air atmosphere. The particle size distribution is between 100 and 300 μm.

2.2. Experimental Set-UP

The oxygen carrier performances were investigated during oxidation/reduction cycles. These cycles were carried out in a fixed bed reactor previously described in the literature [22]. The oxygen carrier was placed inside a quartz tubular reactor (6 mm inner diameter). The bed thickness of the oxygen carrier was around 5 mm. The fixed bed reactor was heated by a tubular furnace (Pekly/Herrmann-Moritz, Thiron Gardais, France). The experiments were performed between 700 and 900 °C. Two thermocouples were above and below the fixed bed and allowed estimating the temperature within the bed. Mass flow controllers (BROOKS 5850, Brooks Instrument, Hatfield, PA, USA) maintained the gas flow rate in the reactor (20 to 50 $NL{\cdot}h^{-1}$) during the experimental tests. Reduction experiments were performed with carbon monoxide C_0 = 0.1 to 1 vol % in nitrogen. After the reduction step, the oxygen carrier was re-oxidized under air at the same operating conditions than the reduction ones. The gases coming out from the reactor (CO, CO_2 and O_2) were continuously analyzed by an NG2000 infrared analyzer (for CO and CO_2, concentration inferior to 1 vol %, Edinburgh Instruments Ltd, Livingston, UK) and by a paramagnetic Rosemount X-stream analyzer (for oxygen, range 0–20 vol %, Rosemount Analytical Inc, Anaheim, CA, USA). A data acquisition system recorded in real time the experimental data.

2.3. Experimental Design

First, the oxygen carrier was heated from room to operating temperature under nitrogen. Then, a mixture of carbon monoxide in nitrogen was injected at the reactor inlet (reduction step). This step was assumed complete when CO concentrations at the reactor inlet and outlet were the same. Before regenerating the oxygen carrier, pure nitrogen was injected (inerting operation, 10 min). The oxidation of the oxygen carrier was performed under air and at the same operating conditions (temperature, flow rate ...). Before starting a new reduction -oxidation cycle an inerting step was performed to avoid risks related to the presence of oxidant gas and reductant gas at the same time in the reactor.

2.4. Sample Characterizations

Scanning Electron Microscopy (SEM) experiments were performed on both fresh oxygen carrier and aged samples using a XL30 FEG Microscope (Philips, Andover, MA, USA) equipped with an Oxford Inca Si (Li) (Oxford Instruments, Concord, MA, USA) energy dispersive X-ray spectrometer (EDX). In addition, the different samples were characterized by X-ray Diffraction (XRD) using an X'Pert Pro diffractometer (PAN Analytical, Almelo, Netherlands) operating with Cu Kα radiation (λ = 0.15418 nm) equipped with a X'Celerator detector. XRD investigation was performed for 2θ angles in the 10–90° range (step of 0.02°).

3. Numerical Part

3.1. Kinetic Models

Several kinetic models were considered to study the behavior of the oxygen carrier under reducing conditions. Two model categories are mainly used in the literature to simulate CLC processes [15].

The most-used models are the unreacted shrinking core model (SCM), the modified volumetric model (MVM) and the nucleation growth model (NGM) [23–25]. In particular, these investigations used and compared the different models to each other for simulating different CLC processes. Indeed, Han et al. [25] investigated the oxidation of hydrogen by a Ni-based oxygen carrier in TGA apparatus. These authors studied the effect of particle size to examine the diffusion limitation, the effect of cyclic testing and the binder reactivity.

These models allow estimating the conversion yield (X) of the oxygen carrier. This conversion yield can be defined as follows:

$$X = \frac{nO(t=0) - nO(t)}{nO(t=0) - nO(t \to \infty)} \tag{1}$$

The unreacted shrinking core model takes into account the particle size and the pore structure [26–28]. The kinetic is governed by three limiting phenomena; diffusion in the external gas film, diffusion into particles, and chemical reaction [26,29]. Several authors [29,30] neglected the external transfer term in the shrinking core model. According to these hypotheses, the conversion yield can be calculated by solving the following equation:

Shrinking Core Model (SCM):

$$t = \frac{1}{k_c[CO]^n}(1-(1-X)^{\frac{1}{3}}) + \frac{1}{k_d[CO]^n}\left(1+2(1-X)-3(1-X)^{\frac{2}{3}}\right) \tag{2}$$

where k_c and k_d are the kinetic constants relative to chemical reaction and diffusion respectively, $[CO]$ is the carbon monoxide concentration. This equation is the sum of two contributions: a convective one related to the chemical process and a diffusive one related to the diffusion transport limitations.

For modeling fluidized CLC units, some authors neglected transport limitations, assuming that the reaction is fully controlled by the chemical process [31–33].

The second category is volumetric models [34,35]. The more used ones to simulate CLC operation are the volumetric model and nucleation-growth model. The conversion yield can be calculated by solving the following equations.

Nucleation Growth Model (NGM):

$$\frac{dX}{dt} = k.[CO]^n\left(\nu(1-X)\times(-\ln(1-X))^{\frac{\nu-1}{\nu}}\right) \tag{3}$$

Modified Volumetric Model (MVM):

$$t = \frac{1}{k[CO]^n}(-\ln(1-X)) \tag{4}$$

The different kinetic k, k_c and k_d are function of the operating temperature.

3.2. 1D-Unsteady Simulation of the Reaction in the Fixed Bed Reactor

Several fluid dynamic tests (Residence Time Distribution) were performed in the reactor and the results show that the gas flow has a plug flow behavior with axial diffusion [22]. In addition, Peclet number [36] (i.e., ratio of convective transport and diffusive one) is, in the worst case scenario, higher than 30, meaning that convection transport is predominant. In the same way, heat transfer are assumed one dimensional because the reactor is at constant operating temperature and the Damköhler II number [37,38] (i.e., ratio of heat generation rate to convective heat transport) is very small (4×10^{-4} in the worst case scenario). Starting from these assumptions, a 1D-unsteady model was developed [39] to take into account the gradient of oxygen concentration in the reactor and the effect of the flow

on the combustible gas. The numerical modeling requires solving mass balance of combustible gas concentration $C(x,t)$ along the fixed bed thickness:

$$\frac{\partial C}{\partial t} + u\frac{\partial C}{\partial x} = D\frac{\partial^2 C}{\partial x^2} - r(x,t) \quad (5)$$

The oxidation rate of carbon monoxide. $r(x,t)$ is deduced from the unsteady mass balance of available oxygen in the oxygen carrier (Equation (6)), where the conversion $X(x,t)$ is calculated from kinetic equations (Equations (2)–(4) respectively):

$$\frac{1}{V(x)}\frac{\partial nO(x,t)}{\partial t} = -r(x,t) = -\frac{(nO(x,0) - nO(x,\infty))}{V(x)}\frac{\partial X(x,t)}{\partial t} \quad (6)$$

Boundary conditions: $C(x = 0,t) = C_0$; $C(x,t = 0) = 0$. The initial available amount of oxygen used in the calculation is the experimental one. The set of Equations (5), (6), and (2) or (4), is solved by using the finite difference methodology to approximate the axial gradients and the Gear method for time dependence (explicit method with variable time step). The model is written in FORTRAN code.

4. Results and Discussion

4.1. Experiments in Fixed Bed Reactor

The study was carried out with the oxygen carrier $NiO/NiAl_2O_4$ in the fixed bed reactor according to the experimental design (reduction and oxidation step). To investigate the influence of the operating parameters (temperature, CO concentration, mass flow rate and amount of oxygen carrier), several series of tests were performed according to a design of experiments (DOE).

This tool used in many fields [40–42] allows obtaining the maximum of information about the operating parameters influence, from a minimum of tests. In this case, the influence of three reduction parameters was studied (temperature, mass flow rate and ratio between inlet concentration of CO and amount of oxygen available on the oxygen carrier). All the experiments are carried out with the same bed thickness. For this, the oxygen carrier is diluted with SiC particles exhibiting similar granulometry (except for tests 33 and 34) to obtain the same thickness and avoid modifying the fluid dynamic in the reactor. A rotatable central composite design [43] was chosen, it consists in an orthogonal factorial design with two levels, a set of centred points and a set of axial points with a factor outside the studied range. Each experimental test is repeated twice to ensure reproducibility. The numbering of experimental tests follows the chronological sequence of operations (test 1 is performed with fresh oxygen carrier...). Table 1 summarizes the operating conditions and the results of the experimental tests.

Table 1. Experimental tests.

Cycle	T (°C)	Q (NL·h^{-1})	[CO] (vol %)	Ratio (C_0/NiO)	CO Oxidized (mol)	Time $C_{1/2}$(t) = C_0/2 (s)
2	700	40	0.51	2.55	5.47×10^{-4}	200
3	700	40	0.51	2.55	5.40×10^{-4}	200
5	739	28.1	0.22	1.1	5.87×10^{-4}	735
6	739	28.1	0.22	1.1	5.82×10^{-4}	724
7	739	28.1	0.80	4	5.84×10^{-4}	204
8	739	28.1	0.80	4	5.79×10^{-4}	202
9	739	51.9	0.22	1.1	5.61×10^{-4}	373
10	739	51.9	0.22	1.1	5.43×10^{-4}	359
12	739	51.9	0.80	4	5.40×10^{-4}	95
13	739	51.9	0.80	4	5.59×10^{-4}	101
14	800	20.0	0.51	2.55	5.78×10^{-4}	397
15	800	20.0	0.51	2.55	5.88×10^{-4}	408

Table 1. *Cont.*

Cycle	T (°C)	Q (NL·h^{-1})	[CO] (vol %)	Ratio (C_0/NiO)	CO Oxidized (mol)	Time $C_{1/2}(t) = C_0/2$ (s)
16	800	40.0	0.51	2.55	5.96×10^{-4}	233
17	800	40.0	0.51	2.55	5.94×10^{-4}	233
18	800	40.0	1.00	5	6.18×10^{-4}	123
19	800	40.0	1.00	5	6.30×10^{-4}	125
20	800	60.0	0.51	2.55	5.93×10^{-4}	149
21	800	60.0	0.51	2.55	5.92×10^{-4}	148
23	861	28.1	0.80	4	7.15×10^{-4}	259
24	861	28.1	0.80	4	7.11×10^{-4}	255
25	861	28.1	0.22	1.1	7.12×10^{-4}	913
26	861	28.1	0.22	1.1	7.04×10^{-4}	898
27	861	51.9	0.22	1.1	6.62×10^{-4}	457
28	861	51.9	0.22	1.1	6.50×10^{-4}	451
29	861	51.9	0.80	4	6.66×10^{-4}	126
30	861	51.9	0.80	4	6.70×10^{-4}	128
31	900	40.0	0.51	2.55	6.92×10^{-4}	275
32	900	40.0	0.51	2.55	7.13×10^{-4}	284
33	800	40.0	0.1	0.1	7.08×10^{-3}	4643
34	800	40.0	0.1	0.1	7.35×10^{-3}	4800

The C_0/NiO ratio is the ratio of inlet CO concentration (vol %) to the theoretical amount of oxygen available in the OC (SiC dilution ratio).

4.1.1. Effect of Temperature

Figure 1 shows the breakthrough curves of CO obtained during experimental tests n° 2, 16 and 31 performed at 700, 800 and 900 °C, respectively. The other operating conditions are exactly the same. The higher the operating temperature is, the higher the amount of CO oxidized is. Nevertheless, the shape of the curves seems to be unaffected. The integration of the breakthrough curves (oxidized CO or produced CO_2) given in Table 1, column 6 corroborates previous observations.

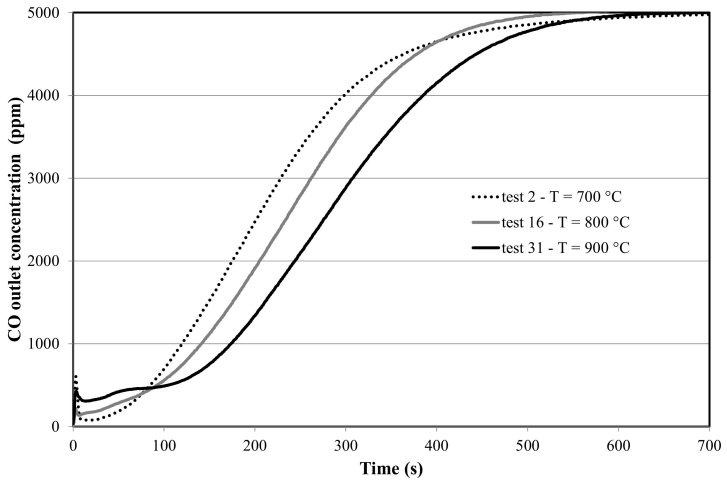

Figure 1. Breakthrough curves of CO obtained during experimental tests performed at different temperatures (700, 800 and 900 °C). Operating conditions: Q = 40 NL/h, ratio C_0/NiO = 2.55.

4.1.2. Effect of Flow Rate

Figure 2 shows the breakthrough curves of CO obtained during experimental tests (tests 14, 16 and 20) performed at different flow rates (20, 40 and 60 NL/h). As expected the higher the flow rate is, the faster the percolation of CO is.

The difference of experimental curves (breakthrough time) obtained at different mass flow rates can be attributed to the fluid dynamic in the fixed bed reactor. Indeed, results from Table 1 show that the amount of produced CO_2 is approximately the same when the flow rate is 20, 40 and 60 NL/h.

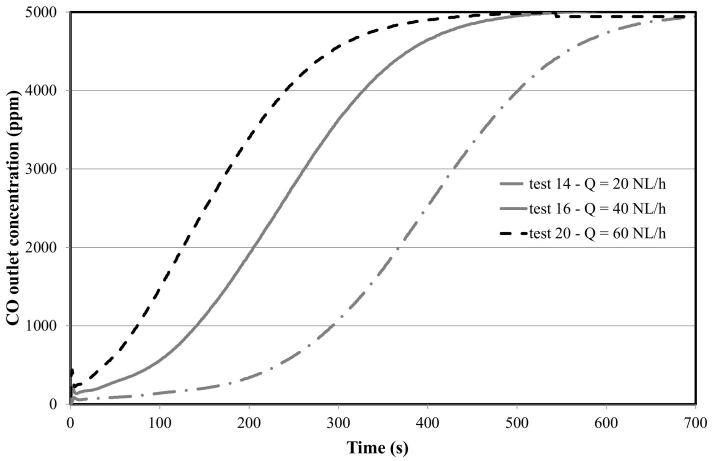

Figure 2. Breakthrough curves of CO obtained during experimental tests (tests 14, 16, 20) performed at different flow rates (20. 40 and 60 NL/h). Operating conditions: T = 800 °C, ratio (C_0/NiO) = 2.55.

4.1.3. Effect of CO/NiO Ratio

Figure 3 shows the breakthrough curves of CO (weighted values) obtained during experimental tests (tests 16, 18 and 33). As expected, the time of the reduction step increases in inverse proportion when the inlet CO concentration decreases and when the amount of available oxygen in the OC increases (i.e., decrease of C_0/NiO ratio). The amount of CO oxidized (or produced CO_2) during the three studied reduction cycles (Table 1) weighted by the mass of metal oxide introduced in the reactor is 6.39 mol·kg^{-1} for test 18 (R = 5), 6.16 mol·kg^{-1} for test 16 (R = 2.55) and 6.99 mol·kg^{-1} for test 33 (R = 0.1) respectively. This parameter does not seem to modify the reduction total capacity of the oxygen carrier, but it affects the time of trial performing.

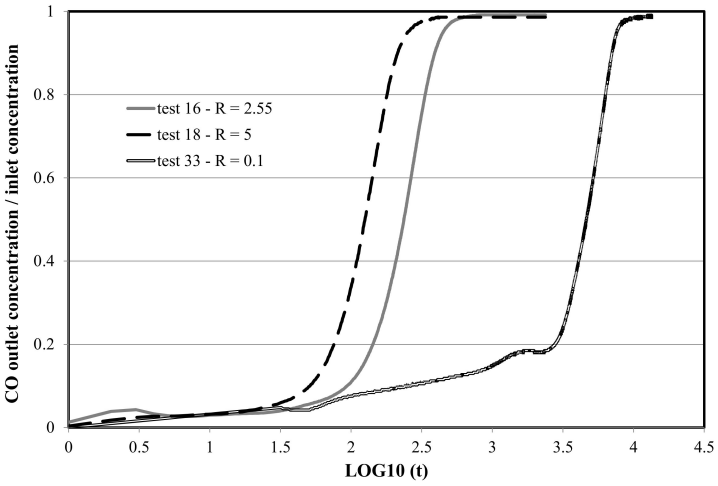

Figure 3. Outlet concentrations of CO (weighted by the inlet CO concentration) obtained during experimental tests performed vs. time (common logarithm base 10) for different ratio (C_0/NiO) (R = 0.1, 2.55 and 5). Operating conditions: T = 800 °C, Q = 40 NL/h.

4.2. Reaction Modeling in the Fixed Bed (1D-Unsteady Approach)

The simulations are performed by solving mass balances (for combustible Equation (5) and for oxygen carrier Equation (6)) with the three studied kinetic models (the volumetric model is a specific case of the nucleation model ν = 1). The geometrical and operative conditions used for numerical calculation are reported in Table 2. The kinetic parameters are adjusted to fit experimental results by minimizing a quadratic criterion (quadratic error between experimental and simulated results). The plot of the estimated constant for the two models versus the inlet combustible concentration (in a log log diagram) gives linear curves with a slope close to 1 (partial reaction order).

Table 2. Geometrical and operating conditions use for simulations.

Reactor and Oxygen Carrier	Operating Conditions
Bed length = 5 mm	Fuel = carbon monoxide in nitrogen
Oxygen carrier = $NiO/NiAl_2O_4$ (60/40 wt %.)	Inlet CO concentration = 0.1 to 1 vol %.
Dilution OC (ratio = 1 to 5 with SiC)	$20 \leq Q \leq 60$ NL·h^{-1}
Available mole of oxygen (nO (t = 0)) = experimental one	$700 \leq T \leq 900$ °C

Figure 4 shows the experimental and numerical results obtained for test 16 (CO breakthrough curves) with the Shrinking Core Model. Numerical results obtained with the Shrinking Core Model cannot satisfactorily approximate the experimental results. Indeed, to have a complete oxidation of CO at the beginning (i.e., the concentration of CO at the reactor outlet is quasi null at $t = 0^+$) and the model required to input a constant k_c value higher than 0.032 mol^{-1} s^{-1} (example: test 16 on Figure 5) and a constant $k_d >> k_c$. For these values of kinetic constants, the slope of the simulated breakthrough curves at the inflexion point is too steep and this cannot fit with experimental results. k_c value increases the initial conversion and the slope of the curve at the inflexion point while a decrease of k_d value tends to decrease this slope and the initial conversion.

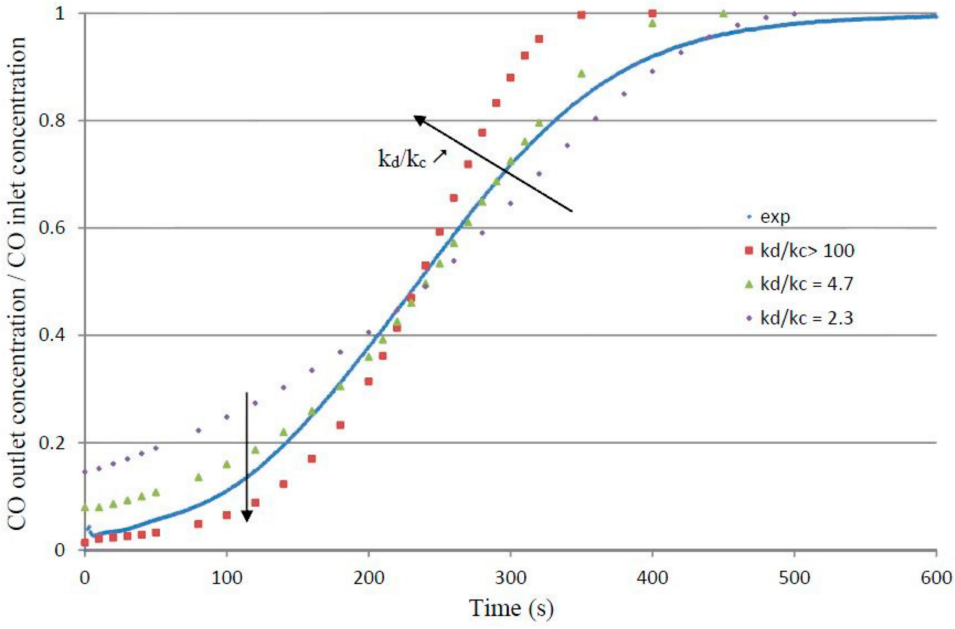

Figure 4. Experimental and simulated (SCM) CO breakthrough curves; k_c = 0.032 mol^{-1}·s^{-1}, test 16.

Similarly, simulations performed with the nucleation growth model highlight the same problems. Figure 5 shows the experimental and simulated CO breakthrough curves. Figure 5a shows the experimental (cycle 16) and numerical results obtained by varying the kinetic constant. It increases

the initial conversion and the slope of the curve at the inflexion point. Indeed, the numerical model can approximate the beginning or the end of the breakthrough curves, but not both. Figure 5b shows the same experimental results with simulated ones performed by varying the Avrami coefficient. It modifies the shape of the breakthrough curve (i.e., modifications of the reaction mechanisms). To conclude, the two studied models cannot model and predict adequately the gas-solid reaction.

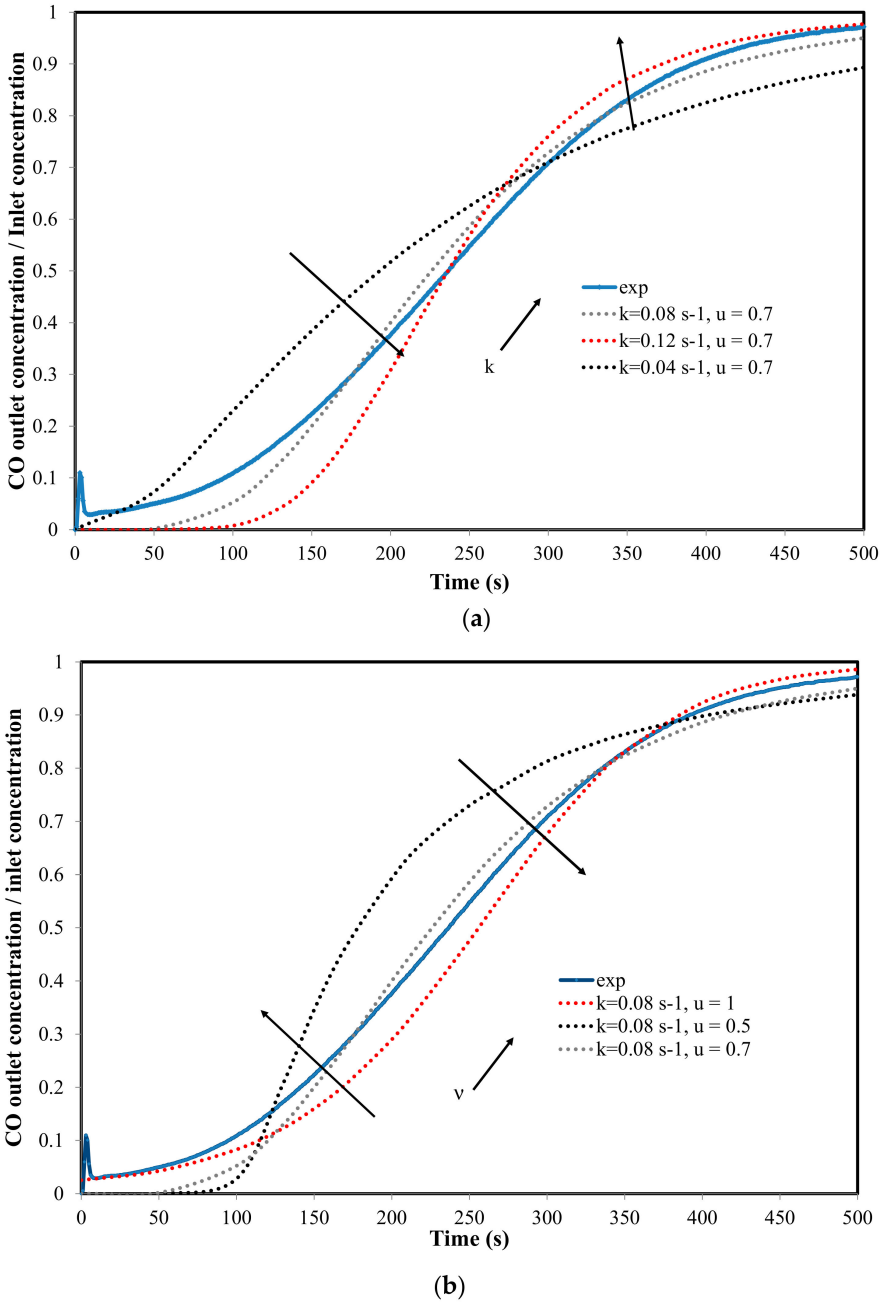

Figure 5. Experimental and simulated results (cycle 16) by (**a**) varying the kinetic constant and (**b**) the Avrami coefficient.

Microscopy investigation shows that some particles of aged material are sintered. Moreover, a light grey layer covers the aged particles (Figure 6). Previous investigations (SEM, XRD) have shown that this layer is rich in nickel [14], probably due to the migration of nickel to the particles' surface as cycles are performed.

The initial particles (fresh material) are near-spherical and the nickel oxide is homogeneously dispersed. After several cycles, the particles are covered by nickel oxide (powerful oxidizing agent) directly available by convection. The rest of the nickel oxide is in the core of the particles and is accessible only by combustible diffusion in the particle. So, the beginning of the reaction seems to be controlled by chemical limitation and subsequently the reaction is limited by diffusion mechanisms inside the particle.

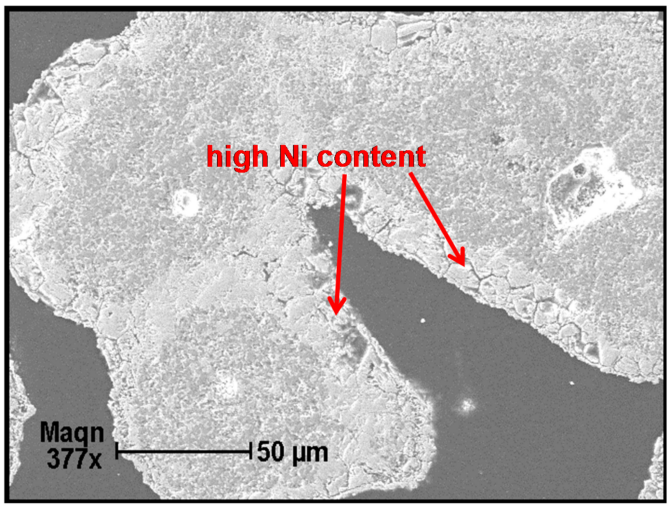

Figure 6. SEM photograph of oxygen carrier particle after 2 cycles at 900 °C.

From these observations, it seems that different reaction sites may take part in the global oxygen carrier reactivity. The oxidant available in the oxygen carrier is divided in two site types, the first one noted, indicated by (1), is nickel oxide at the particles' surface, where the reaction with fuel is solely controlled by chemical limitation. The remaining NiO (2) reacts with fuel after diffusion inside the particle (Equation (7)). To illustrate these assumptions, Figure 7 shows a SEM-EDX photograph of the material after several cycles performed at 739 °C.

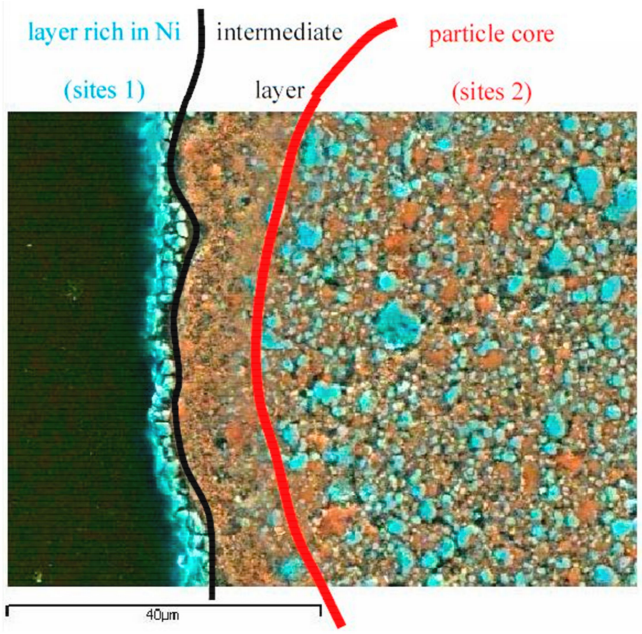

Figure 7. SEM-EDX photograph of OC particle (Ni in blue and Al in orange).

The intermediate layer is low in nickel. This layer is impoverished in nickel for the benefit of the surface layer. It reduces the accessibility to the oxygen carrier in the core of the particle.

Image processing carried out on different particles evaluates that around 20% of NiO is in the surface layer:

$$\frac{\partial nO}{\partial t} = \frac{\partial nO1}{\partial t} + \frac{\partial nO2}{\partial t} = -nO1(0).\frac{\partial X_1}{\partial t} - (nO2(0) - nO(\infty))\frac{\partial X_2}{\partial t} \quad (7)$$

The amount of nickel oxide ($nO1$) available at the particles' surface is assumed 20% of the oxidant. As for previous simulations, the total amount of available oxygen nO (t = 0) is the experimental one. The kinetic models are respectively (Equation (8)):

$$\begin{gathered} t = \frac{1}{k_{c1}[CO]^n}(1-(1-X_1)^{\frac{1}{3}}) \text{ and} \\ t = \frac{1}{k_{c2}[CO]^n}(1-(1-X_2)^{\frac{1}{3}}) + \frac{1}{k_d[CO]^n}\left(1+2(1-X_2)-3(1-X_2)^{\frac{2}{3}}\right) \end{gathered} \quad (8)$$

This new numerical approach introduces an additional parameter, which leads to different solutions in term of quadratic error minimization. To estimate the kinetic parameters, a mixed criterion was used. It is the pondered sum of three criteria; the quadratic error for all tests, the error on the initial conversion and the first derivative value at $\frac{C_0}{2}$ (inflection point of the breakthrough curve). All the experimental tests have been simulated and the best-fitted parameters are: k_{c1} = 0.061 mol^{-1} s^{-1}, k_{c2} = 0.032 mol^{-1} s^{-1}, k_d = 0.1 mol^{-1} s^{-1} and n = 1.

In this case, a same set of parameters is able to simulate all the experimental tests. As previous results obtained, the partial reaction order is close to 1. Figure 8 shows the breakthrough curves (experimental and simulated) for test 16 and test 18 (T = 800 °C, Q = 40 NL/h). The simulated fuel concentrations obtained with these parameters are in a good agreement with experimental results.

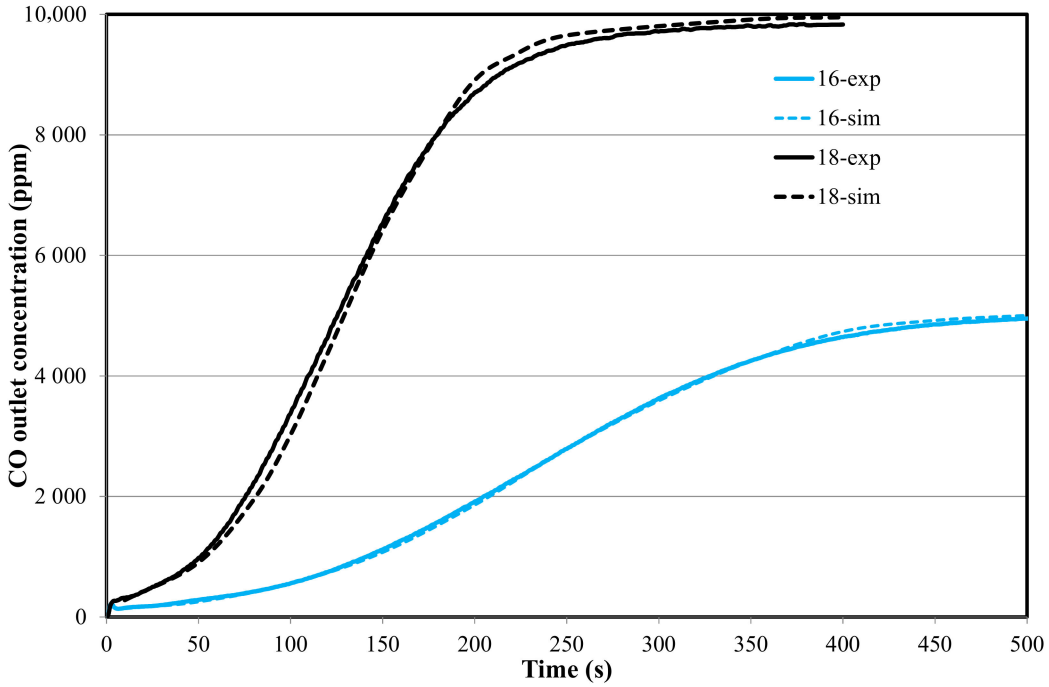

Figure 8. Experimental and simulated breakthrough curves for test 16 (ratio C_0/NiO = 2.55) and for test 18 (ratio C_0/NiO = 5). Operating conditions: T = 800 °C and Q = 40 NL/h.

The 1D-modelling takes into account the influence of the flow dynamics in the reactor. Figure 9 shows experimental and simulated breakthrough curves for tests 14 and 20. These two tests are performed at 800 °C and C_0/NiO = 2.55. The flow rate is 20 NL/h and 60 NL/h for tests 14 and 20 respectively. These results as well as those related to tests 16 and 18 (previous figure) show that the numerical modeling is better able to simulate the effect of convective transport.

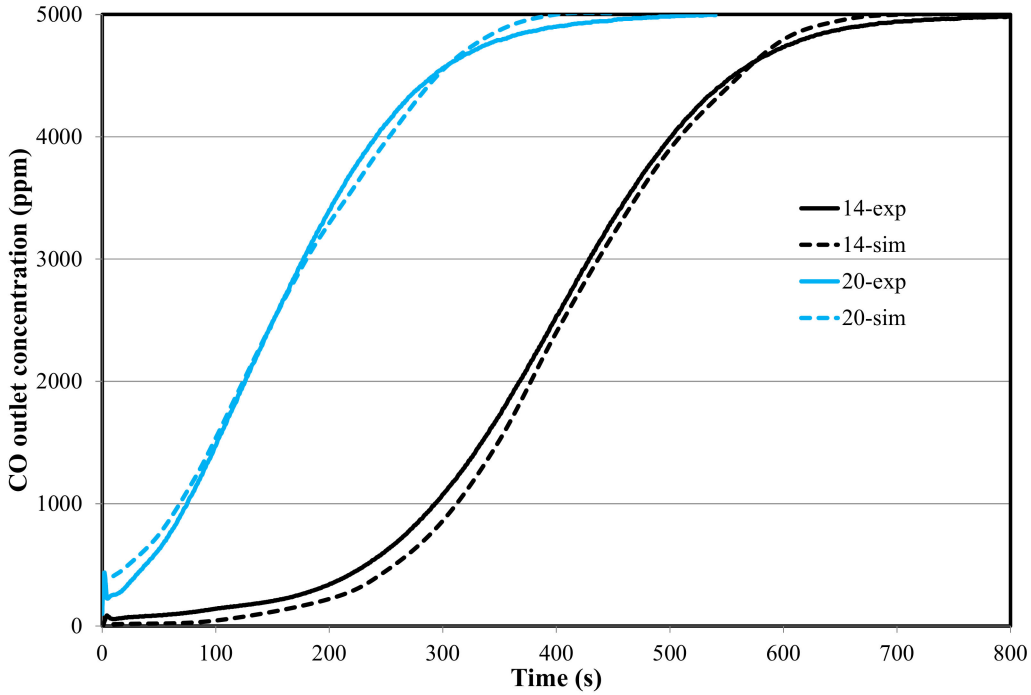

Figure 9. CO concentrations at the reactor outlet versus time for tests 14 (Q = 20 NL/h) and 20 (Q = 60 NL/h). Operating conditions: T = 800 °C and C_0/NiO = 2.55.

Most striking of all, however, is the non-dependence of the kinetics on operating temperature. Indeed the optimal kinetic parameters are not function of the temperature in the studied range. Nevertheless, the total capacity of reduction (i.e., the total amount of available oxygen) increases with temperature as shown in Table 1. These results are in agreement with previous results [22] showing chemical control of the reaction in this range of temperature. Figure 10 shows the experimental breakthrough curves carried out at 700 and 900 °C. As with the test at 800 °C (test 14), the simulations are in good agreement with the experimental results. The difference between the two curves is only due to the difference of initial amount of available oxygen (5.4×10^{-4} mol for test 2 and 7.0×10^{-4} mol for test 31).

These results can be partially explained by the competition between kinetics and mass transfer. Indeed, the limitation is only due to accessibility to the reactive sites and the effect of operating temperature is obscured by mass transfer limitations inside the particles. To observe the temperature influence, experimental tests should be performed at high flow rates (i.e., with immediate percolation of the combustible gas). At the same time, the increase of overall oxidized CO with temperature is certainly due to the separation of the binder ($NiAl_2O_4$) phase to NiO and Al_2O_3, as previously observed [11].

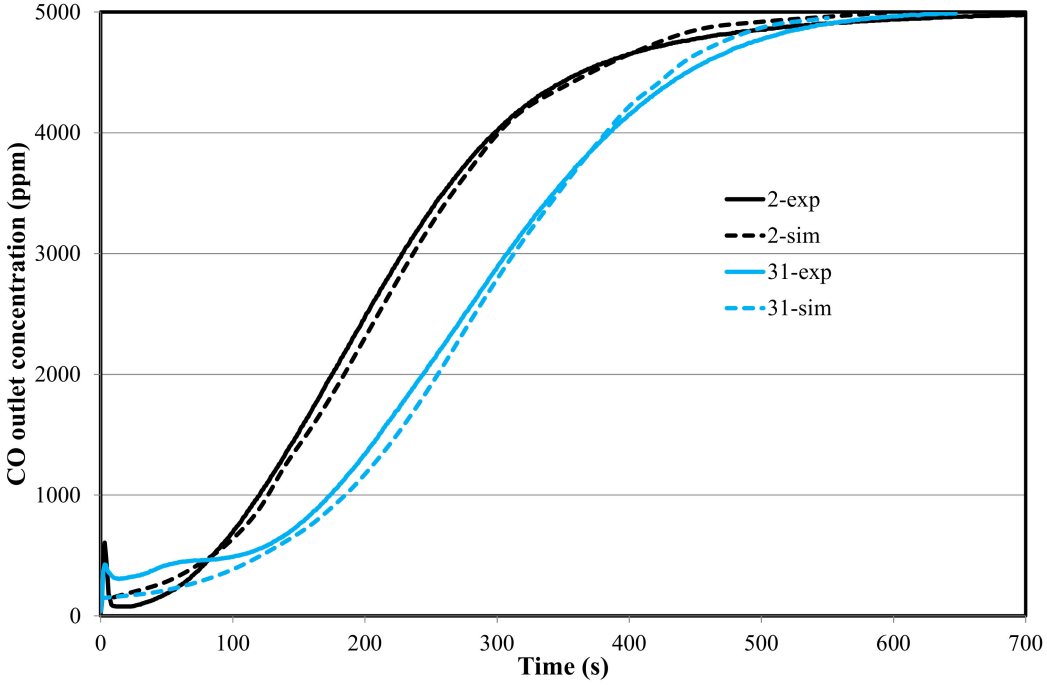

Figure 10. Breakthrough curves (experimental and simulated) for test 2 (700 °C) and test 31 (900 °C). Operating conditions: Q = 40 NL/h and C_0/NiO = 2.55.

5. Conclusions

Experimental results from fixed bed reactor (fuel breakthrough curves) are investigated by using different kinetic modeling methods. First, the kinetic modeling is unable to well describe the experimental results. The integration of the kinetic model in a 1D mass transfer modeling improves slightly the model fitting. Observations of the oxygen carrier after several cycles of oxidation reduction show the formation of a high nickel content layer at the OC surface. This layer promotes aggregation and particle sintering. In this way, the numerical investigation suggests to decompose the oxygen carrier active sites in two types. The first corresponds to the chemical control of the reaction (nickel oxide at the surface of the particles) and the second to the accessibility to the oxygen carrier in the core of the particle. Starting with these hypotheses, the experimental CO breakthrough curves from all the studied tests are well approximated by the numerical modeling. This good agreement and the results from microscopy support the assumptions of two reaction sites. Moreover, the set of kinetic parameters obtained for all the studied experiments is independent of the operating temperature, which means that mass transfer controls the reaction and occurs the effect of temperature.

Author Contributions: All authors contributed equally to the work done

Conflicts of Interest: The authors declare no conflict of interest.

Nomenclature

Latin letters

C	CO concentration (mol·m^{-3})
D	Diffusion coefficient (m^2·s^{-1})
k	Kinetic constant ((mol·m^{-3})$^{-n}$·s^{-1})
n	Reaction order
nO	Available mole of oxygen in OC (mol)
Q	Flow rate (NL h^{-1})
r(*x*,*t*)	Reaction rate (mol m^{-3} s^{-1})
T	Temperature (°C)

t	Time (s)
u	Average velocity (m s^{-1})
$V(x)$	Discretized volume of the bed (m^3)
x	Coordinate (m)
X	Conversion yield
Greek letters	
ν	Avrami coefficient
Subscript	
0	inlet reactor
1	site 1
2	site 2
c	chemical reaction
d	diffusion
∞	end of experiment

References

1. Intergovernmental Panel on Climate Change (IPCC). *Climate Change 2013: The Physical Science Basis, Firth Assessment Report*; Cambridge University Press: Cambridge, UK, 2013.
2. Liu, C.; Li, X. Carbon storage and sequestration by urban forests in Shenyang, China. *Urban For. Urban Green.* **2012**, *11*, 121–128. [CrossRef]
3. IPCC Guidelines. Chapter 5: Carbon dioxide transport, injection and geological storage. In *2006 IPCC Guidelines for National Greenhouse Gas Inventories*; Cambridge University Press: Cambridge, UK, 2006.
4. Ishida, M.; Jin, H. A new advanced power-generation system using chemical-looping combustion. *Energy* **1994**, *19*, 415–422. [CrossRef]
5. Ishida, M.; Zheng, D.; Akehata, T. Evaluation of a chemical-looping-combustion power-generation system by graphic exergy analysis. *Energy* **1987**, *12*, 147–154. [CrossRef]
6. Lyngfelt, A.; Leckner, B.; Mattisson, T. A fluidized-bed combustion process with inherent CO_2 separation; application of chemical-looping combustion. *Chem. Eng. Sci.* **2001**, *56*, 3101–3113. [CrossRef]
7. Lyngfelt, A. Chemical-looping combustion of solide fuels–Status of development. *Appl. Energy* **2014**, *113*, 1869–1873. [CrossRef]
8. Wang, P.; Means, N.; Shekhawat, D.; Berry, D.; Massoudi, M. Chemical-Looping Combustion and gasification of coals and oxygen carrier development: A brief review. *Energies* **2015**, *8*, 10605–10635. [CrossRef]
9. Bhave, A.; Taylor, H.S.; Fennell, P.; Livingston, W.R.; Shah, N.; Mac Dowell, N.; Dennis, J.; Kraft, M.; Pourkashanian, M.; Insa, M.; et al. Screening and techno-economic assessment of biomass-based power generation with CCS technologies to meet 2050 CO_2 targets. *Appl. Energy* **2017**, *190*, 481–489. [CrossRef]
10. Noorman, S.; van Sint Annaland, M.; Kuipers, J.A.M. Experimental validation of packed bed chemical-looping combustion. *Chem. Eng. Sci.* **2010**, *65*, 92–97. [CrossRef]
11. Blas, L.; Dutournié, P.; Dorge, S.; Josien, L.; Kehrli, D.; Lambert, A. Thermal stability study of $NiAl_2O_4$ binders for Chemical-Looping Combustion application. *Fuel* **2016**, *182*, 50–56. [CrossRef]
12. Dueso, C.; Abad, A.; García-Labiano, F.; de Diego, L.F.; Gayán, P.; Adánez, J.; Lyngfelt, A. Reactivity of a NiO/Al_2O_3 oxygen carrier prepared by impregnation for chemical-looping combustion. *Fuel* **2010**, *89*, 3399–3409. [CrossRef]
13. Gayán, P.; de Diego, L.F.; García-Labiano, F.; Adánez, J.; Abad, A.; Dueso, C. Effect of support on reactivity and selectivity of Ni-based oxygen carriers for chemical-looping combustion. *Fuel* **2008**, *87*, 2641–2650. [CrossRef]
14. Blas, L.; Dorge, S.; Michelin, L.; Dutournié, P.; Lambert, A.; Chiche, D.; Bertholin, S. Influence of the regeneration conditions on the performances and the microstructure modifications of $NiO/NiAl_2O_4$ for chemical looping combustion. *Fuel* **2015**, *153*, 284–293. [CrossRef]
15. Hossain, M.M.; de Lasa, H.I. Chemical-looping combustion (CLC) for inherent separations—A review. *Chem. Eng. Sci.* **2008**, *63*, 4433–4451. [CrossRef]

16. Ohlemüller, P.; Alobaid, F.; Gunnarson, A.; Ströhle, J.; Epple, B. Development of a porous model for coal chemical looping combustion and validation against 100 kWth tests. *Appl. Energy* **2015**, *157*, 433–448. [CrossRef]
17. Wang, X.; Jin, B.; Zhang, Y.; Liu, X. Three dimensional modelling of a coal-fired chemical looping combustion process in the circulating fluidized bed fuel reactor. *Energy Fuels* **2013**, *27*, 2173–2184. [CrossRef]
18. Alobaid, F.; Ohlemüller, P.; Ströhle, J.; Epple, B. Extended Euler-Euler model for the simulation of a 1 MWth chemical-looping pilot plant. *Energy* **2015**, *93*, 2395–2405. [CrossRef]
19. Han, L.; Bollas, G.M. Chemical-looping combustion in a reverse flow fixed bed reactor. *Energy* **2016**, *102*, 669–681. [CrossRef]
20. Diglio, G.; Bareschino, P.; Mancusi, E.; Pepe, F. Novel quasi authermal hydrogen production process in a fixed-bed reactor using a chemical looping approach: A numerical study. *Int. J. Hydrog. Energy* **2017**, *42*, 15010–15023. [CrossRef]
21. Liang, Z.; Qin, W.; Dong, C. Experimental and Theoretical Study of the Interactions between Fe_2O_3/Al_2O_3 and CO. *Energies* **2017**, *10*, 598. [CrossRef]
22. Blas, L.; Dorge, S.; Dutournié, P.; Lambert, A.; Chiche, D.; Bertholin, S.; Josien, L. Study of the performances of an oxygen carrier: Experimental investigation of the binder's contribution and characterization of its structural modifications. *Comptes Rendus Chim.* **2015**, *18*, 45–55. [CrossRef]
23. Zhou, Z.; Han, L.; Bollas, G.M. Kinetics of NiO reduction by H_2 and Ni oxidation at conditions relevant to chemical-looping combustion and reforming. *Int. J. Hydrog. Energy* **2014**, *39*, 8535–8556. [CrossRef]
24. Iliuta, I.; Tahoces, R.; Patience, G.S.; Rifflart, S.; Luck, F. Chemical-looping combustion process: Kinetics and mathematical modelling. *AIChE J.* **2010**, *56*, 1063–1079. [CrossRef]
25. Han, L.; Zhou, Z.; Bollas, G.M. Model-based analysis of chemical-looping combustion experiments. Part II: Optimal design of CH_4-NIO reduction experiments. *Chem. Eng. Sci.* **2014**, *113*, 116–128. [CrossRef]
26. Ishida, M.; Jin, H.; Okamoto, T. A fundamental study of a new kind of medium material for chemical looping combustion. *Energy Fuels* **1996**, *10*, 958–963. [CrossRef]
27. Utigard, T.A.; Wu, M.; Plascencia, G.; Marin, T. Reduction kinetics of goro nickel oxide using hydrogen. *Chem. Eng. Sci.* **2005**, *60*, 2061–2068. [CrossRef]
28. Dueso, C.; Ortiz, M.; Abad, A.; García-Labiano, F.; de Diego, L.F.; Gayán, P.; Adánez, J. Reduction and oxidation kinetics of nickel-based oxygen-carriers for chemical-looping combustion and chemical-looping reforming. *Chem. Eng. J.* **2012**, *188*, 142–154. [CrossRef]
29. Ryu, H.J.; Bae, D.H.; Han, K.H.; Lee, S.Y.; Jin, G.T.; Choi, J.H. Oxidation and reduction characteristics of oxygen carrier particles and reaction kinetics by unreacted core model. *Korean J. Chem. Eng.* **2001**, *18*, 831–837. [CrossRef]
30. Hossain, M.M.; de Lasa, H. Reduction and oxidation kinetics of Co-Ni/Al_2O_3 oxygen carrier involved in a chemical-looping combustion cycles. *Chem. Eng. Sci.* **2010**, *65*, 98–106. [CrossRef]
31. Garcia-labiano, F.; de Diego, L.F.; Adanez, J.; Abad, A.; Gayan, P. Reduction and oxidation kinetics of a copper-based oxygen carrier prepared by impregnation for chemical looping combustion. *Ind. Eng. Chem. Res.* **2004**, *43*, 8168–8177. [CrossRef]
32. Hossain, M.M.; de Lasa, H. Reactivity and stability of Co-Ni/Al_2O_3 oxygen carrier in multicycle chemical-looping combustion. *AIChE J.* **2007**, *53*, 1817–1829. [CrossRef]
33. Kruggel-Emden, H.; Rickelt, S.; Stepanek, F.; Munjiza, A. Development and testing of an interconnected multiphase CFD-model for chemical looping combustion. *Chem. Eng. Sci.* **2010**, *65*, 4732–4745. [CrossRef]
34. Richardson, J.T.; Scates, R.M.; Twigg, M.V. X-ray diffraction of hydrogen reduction of NiO: α-Al_2O_3 steam reforming catalysts. *Appl. Catal. A* **2004**, *267*, 35–46. [CrossRef]
35. Gomez-Barea, A.; Ollero, P. An approximate method for solving gas-solid non-catalytic reactions. *Chem. Eng. Sci.* **2006**, *61*, 3725–3735. [CrossRef]
36. Bird, R.B.; Stewart, W.E.; Ligthfoot, E.N. *Transport Phenomena*, 2nd ed.; J. Wiley & Sons: New York, NY, USA, 2007.
37. Annamalai, K.; Puri, I.K. *Combustion Science and Engineering*; CRC Press: New York, NY, USA, 2007.
38. Diglio, G.; Bareschino, P.; Mancusi, E.; Pepe, F. Simulation of hydrogen production through chemical looping reforming process in a packed-bed reactor. *Chem. Eng. Res. Des.* **2016**, *105*, 137–151. [CrossRef]
39. Noorman, S.; Gallucci, F.; Annaland, M.V.; Kuipers, J.A.M. A theoretical investigation of CLC in packed beds. Part 2: Reactor model. *Chem. Eng. J.* **2011**, *167*, 369–376. [CrossRef]

40. Valencia, P.; Espinosa, K.; Ceballos, A.; Pinto, M.; Almonacid, S. Novel modeling methodology for the characterization of enzymatic hydrolysis of proteins. *Proc. Biochem.* **2015**, *50*, 589–597. [CrossRef]
41. Dutournié, P.; Salagnac, P.; Glouannec, P. Optimization of radiant-convective Drying of a porous medium by design of experiment methodology. *Dry. Technol.* **2006**, *24*, 953–963. [CrossRef]
42. Lam, J.; Carmichael, S.T.; Lowry, W.E.; Segura, T. Hydrogel design of experiments methodology to optimize hydrogel for iPSC-NPC culture. *Adv. Healthc. Mat.* **2015**, *4*, 534–539. [CrossRef] [PubMed]
43. Hinkelmann, K.; Kempthorne, O. *Design and Analysis of Experiments, Introduction to Experimental Design*, 2nd ed.; Wiley: Hoboken, NJ, USA, 2008.